Inorganic Chemistry

pubs.acs.org/IC

Article

Anomalous Ferromagnetic Behavior in Orthorhombic $Li_3Co_2SbO_6$

Qianhui Duan,[#] Huanpeng Bu,[#] Vladimir Pomjakushin, Hubertus Luetkens, Yuke Li,* Jinkui Zhao, Jason S. Gardner, and Hanjie Guo*

Cite This: *Inorg. Chem.* 2022, 61, 10880−10887

Read Online

ACCESS | Metrics & More | Article Recommendations | Supporting Information

ABSTRACT: Monoclinic $Li_3Co_2SbO_6$ has been proposed as a Kitaev spin liquid candidate and investigated intensively, whereas the properties of its polymorph, the orthorhombic phase, are less known. Here we report the magnetic properties of orthorhombic $Li_3Co_2SbO_6$ as revealed by dc and ac magnetic susceptibility, muon spin relaxation (μSR), and neutron diffraction measurements. Successive magnetic transitions at 115, 89, and 71 K were observed in the low-field dc susceptibility measurements. The transitions below T_N (115 K) are suppressed at higher applied fields. However, zero-field ac susceptibility measurements reveal distinct frequency-independent transitions at about 114, 107, 97, 79, and 71 K. A long-range magnetic ordered state was confirmed by specific heat, μSR, and neutron diffraction measurements, all indicating a single transition at about 115 K. The discrepancy between different measurements is attributed to possible stacking faults and/or local disorders of the ferromagnetic zigzag chains, resulting in ferromagnetic boundaries within the overall antiferromagnetic matrix.

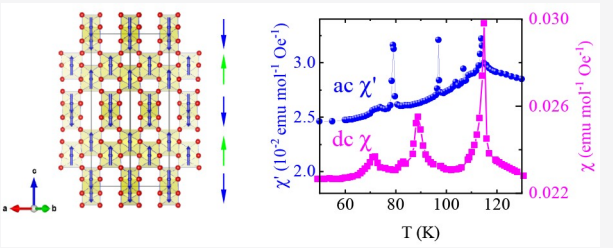

INTRODUCTION

Co^{2+}-based honeycomb lattice materials are of great interest due to the possible realization of the Kitaev model.[1−10] The 3d electrons are more localized compared to those of the 4d (Ru) or 5d (Ir) systems and could suppress the undesired long-range interactions beyond the nearest neighbors. Moreover, the extra e_g electrons introduce more interaction channels which can be tuned to effectively quash the non-Kitaev terms in the Hamiltonian.[5] Such candidates include $A_3Co_2SbO_6$ and $A_2Co_2TeO_6$ (where A is an alkali metal). Among these, $Li_3Co_2SbO_6$ has two polymorphs; one crystallizes in the monoclinic structure with the Co honeycomb lattice and the other in the orthorhombic structure.[11] In the monoclinic phase, the Co−O−Co angle is close to 90°, making this material a better approximation to the Kitaev model than the well-studied $RuCl_3$[12] or Na_2IrO_3.[13] Recent neutron powder diffraction measurements on monoclinic $Li_3Co_2SbO_6$ confirm the formation of ferromagnetic honeycomb layers which stack antiferromagnetically along the *c*-direction.[14] On the other hand, the orthorhombic phase is less investigated.

The main feature of the crystal structure of orthorhombic $Li_3Co_2SbO_6$ can be viewed as a stacking of Co−O zigzag chains along the *c*-axis. The chains, from layer to layer, run along the [110] and [1−10] directions alternatively, as shown in Figure 1a. The Co ions along the chain are connected via edge-shared CoO_6 octahedra, while the interchain Co ions are connected via corner-shared CoO_6 octahedra. The intra- and interchain Co−O−Co angles are about 92° and 170°, presumably leading to antiferromagnetic and ferromagnetic interactions, respectively. Previous studies by Brown et al. have shown that the sample has three transitions at 113, 80, and 60 K, as revealed by dc magnetic susceptibility measurements. Similar multiple transitions in the dc magnetic susceptibility below T_N have been observed in the honeycomb phase such as that in $Na_2Co_2TeO_6$.[3,10] Also, the honeycomb phase of $Li_3Co_2SbO_6$ clearly shows a bifurcation at ∼75 K, well above the antiferromagnetic transition temperature of T_N = 14 K.[11] However, the nature of these multiple transitions remains unclear. Brown et al. have also performed neutron powder diffraction measurements on the title compound but, unfortunately, failed to unravel the magnetic structure of the ordered state.[11] These findings demonstrate the rich properties in the orthorhombic phase, which deserve further investigation.

In order to elucidate the magnetic ground state and the origin of the successive transitions, we have performed detailed dc and ac magnetic susceptibility measurements, together with muon spin relaxation (μSR) and neutron diffraction measurements, which enable us to reveal the underlying magnetic ground state from a microscopic aspect. The most surprising result is the observation of multiple sharp ferromagnetic transitions from the ac susceptibility measurement, which have almost no correspondence in the dc magnetic susceptibility nor in the μSR or neutron measurements. We propose that these

Received: April 18, 2022
Published: July 6, 2022

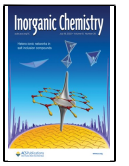

https://doi.org/10.1021/acs.inorgchem.2c01293
Inorg. Chem. 2022, 61, 10880−10887

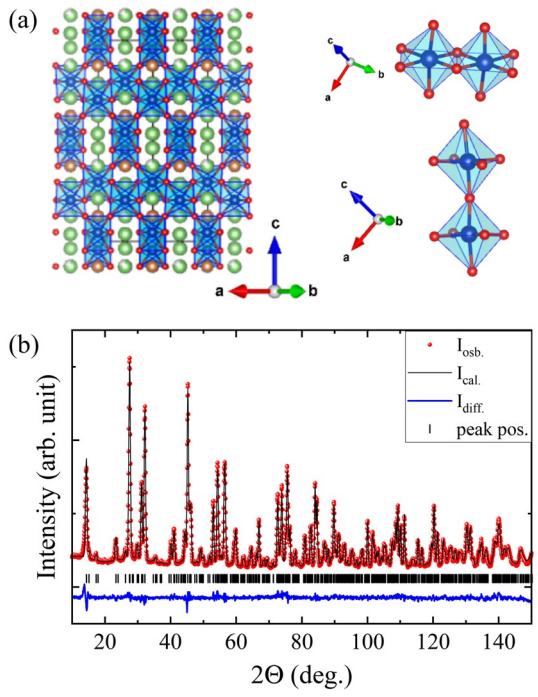

Figure 1. (a) Crystal structure of orthorhombic $Li_3Co_2SbO_6$: blue, Co; red, O; green, Li; yellow, Sb. The local structures of the edge-sharing and corner-sharing CoO_6 octahedra are also shown on the right side. (b) The Rietveld-refined pattern from $Li_3Co_2SbO_6$. The data was collected at 130 K with a neutron wavelength of 1.15 Å.

anomalies most likely originate from the stacking faults and/or local disorders of the zigzag chains, thus forming ferromagnetic regions with a small volume fraction that are difficult to detect by other techniques, but we cannot conclusively rule out other possibilities, like charge fluctuations, spin stripes, or cluster glass dynamics.

EXPERIMENTAL SECTION

Polycrystalline samples of orthorhombic $Li_3Co_2SbO_6$ were prepared by a conventional solid-state reaction method. Li_2CO_3 (99.99%) was dried at 120 °C for 4 h prior to reaction. It was then mixed with Sb_2O_3 (99.99%) in the appropriate ratio to form the Li_3SbO_4 precursor, which was then mixed with stoichiometric amounts of CoO powder and ground thoroughly in an agate mortar, pressed into pellets, and calcined between 1100 and 1150 °C for 24 h, with several intermediate grindings. The phase purity was confirmed both by laboratory X-ray diffraction (XRD) and neutron powder diffraction (NPD) measurements.

The dc and ac magnetic susceptibility measurements were performed using the vibrating sample magnetometer (VSM) and ACMS-II options, respectively, of a physical property measurement system (PPMS DynaCool, Quantum Design). For the ac susceptibility measurement, excitation fields of 5 Oe amplitude are superimposed on various dc bias fields (including zero field). The heat capacity was measured using the relaxation method in the PPMS.

Muon spin relaxation measurements were performed on the GPS spectrometer at the Paul Scherrer Institute (PSI), Villigen, Switzerland. Nearly 100% polarized muons were injected into the sample, and the decayed positrons, which are emitted preferentially along the muon spin direction, were detected. The asymmetry is defined as $A(t) = [N(t) - \alpha B(t)]/[N(t) + \alpha B(t)]$, where $N(t)$ and $B(t)$ are the number of positrons arriving at the forward and backward detectors at time t and the parameter α reflects the relative counting efficiencies of the two detectors. Here, the forward and backward detectors refer to the ones located at the top and bottom positions, respectively, with the muon spin polarization being rotated about 45° with respect to the beam. The data was analyzed using Musrfit software.[15]

Neutron powder diffraction measurements were carried out on the HRPT diffractometer at PSI. Amounts of approximately 10 g of the samples with natural Li were loaded into a vanadium can. Neutron wavelengths of 1.15 and 1.89 Å were used for the nuclear and magnetic structure refinement, respectively. The neutron data was analyzed using the FullProf software suite.[16]

RESULTS

Nuclear Structure. The synthesized sample crystallizes in the orthorhombic phase with space group *Fddd*. Since the laboratory XRD is not sensitive to the light element Li, the nuclear structure refinement was conducted against the NPD pattern collected at 130 K, as shown in Figure 1b. Assuming a full occupancy at each site, it was found that the isotropic thermal parameter, B_{iso}, of Li2 at the 8b site is unusually large. This is consistent with a previous study, where it was assumed that small amounts of Co ions replace the Li ions at this site.[11] However, in this case, some of the Co ions will possess the rare valence state of +1. Therefore, a Li vacancy at the Li2 site is assumed in our refinement, which is reasonable considering the volatile nature of Li at high temperatures. This naturally leads to a mixing of the more common Co^{2+} and Co^{3+} valence states. The refined structural parameters are summarized in Table 1. It was determined that there is a small Li deficiency of ~7% in our sample. In other words, a maximum of about 7% of the Co ions are in the +3 valence state in order to keep charge neutrality.

Magnetic Susceptibility. The temperature dependence of the dc magnetic susceptibility is presented in Figure 2a. A bifurcation can be seen below $T_N \sim 115$ K for the zero-field-cooled (ZFC) and field-cooled (FC) curves, which is most apparent for the 0.1 T data and is gradually suppressed with increasing fields. At 5 T, the two curves almost overlap. A careful inspection of the ZFC curve, as shown in the inset of

Table 1. Structural Parameters of Orthorhombic $Li_3Co_2SbO_6$ Obtained from Rietveld Refinement on the Neutron Data Collected at 130 K with a Neutron Wavelength of 1.15 Å[a]

atom	x	y	z	B_{iso} (Å^2)	occupancy
Li1 (16g)	0.12500	0.62500	0.28578(35)	1.064(98)	1
Li2 (8b)	0.12500	0.62500	0.12500	0.887(165)	0.79(2)
Co (16g)	0.12500	0.12500	0.29475(21)	0.263(46)	1
Sb (8a)	0.12500	0.12500	0.12500	0.294(28)	1
O1 (16g)	0.12500	0.35378(13)	0.12500	0.417(20)	1
O2 (32h)	0.11178(14)	0.37007(18)	0.29559(6)	0.314(10)	1

[a]The space group is *Fddd* (no. 70). The lattice parameters are $a = 5.92526(4)$ Å, $b = 8.68376(6)$ Å, $c = 17.91232(11)$ Å. The *R*-values are $R_p = 8.39\%$ and $R_{wp} = 9.24\%$. The fractional coordinations, isotropic displacement parameters B_{iso}, and the occupancies are presented.

https://doi.org/10.1021/acs.inorgchem.2c01293
Inorg. Chem. 2022, 61, 10880−10887

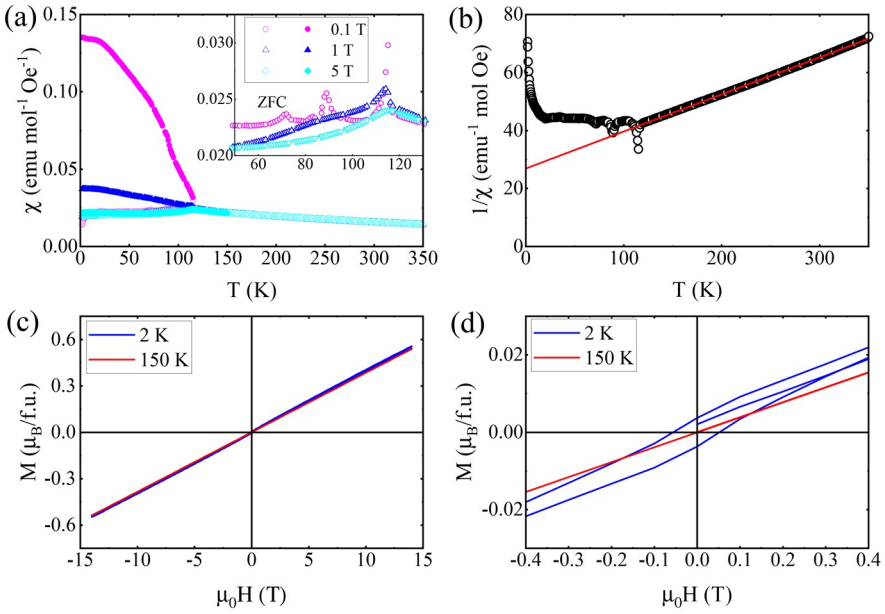

Figure 2. (a) Temperature dependence of the dc magnetic susceptibility measured in the zero-field-cooled (ZFC) and field-cooled (FC) modes, represented by open and closed marks, respectively. The inset highlights the ZFC curve around T_N. (b) Temperature dependence of the inverse magnetic susceptibility χ^{-1} measured with H = 1000 Oe and a fit to the Curie–Weiss law. (c) Isothermal magnetization measurements at various temperatures. (d) A closer look at the hysteresis loop around zero field.

Figure 2a, reveals more complex behavior below T_N. In addition to the peak at ∼115 K, two small peaks appear at ∼89 and ∼71 K, which are also suppressed by the magnetic field and already disappear at 1 T. A Curie–Weiss fit, $\chi^{-1} = (T - \theta_{CW})/C$, to the 0.1 T ZFC curve above 150 K results in an effective moment of 5.60 μ_B/Co and Curie–Weiss temperature, θ_{CW}, of −210 K. The large effective moment indicates that the Co^{2+} ions are in the high-spin state ($S = {}^3/_2$) with a substantial orbital moment.[17] The negative θ_{CW} is suggestive of the dominant antiferromagnetic interactions among Co ions. The bifurcation between the ZFC and FC curves suggests the existence of ferromagnetic components on top of the antiferromagnetic ground state, which is further verified by the isothermal hysteresis measurements. As shown in Figure 2c, the M versus H curves are almost linear down to the lowest temperature, as expected for an antiferromagnet. However, a closer look at the curve in the low-field region clearly shows a hysteresis effect, consistent with the M versus T measurements.

In order to further investigate the nature of the successive transitions below T_N, a series of ac susceptibility measurements have been performed. The samples used for the dc and ac susceptibility measurements shown here are from the same batch, but are not exactly the same ones. Those using exactly the same sample for the dc and ac susceptibility measurements are shown in Figure S1. Figure 3 shows the temperature dependence of the real (χ') and imaginary (χ'') components of the ac susceptibility with various drive frequencies and no dc bias field. Remarkably, at least four sharp peaks (fwhm less than 1 K) can be observed at ∼114, 107, 97, and 79 K both in χ' and χ''. The sharp-peak positions are independent of the frequencies, ruling out the formation of spin glass state.[18] Combined with the presence of a nonzero χ'', these results suggest the presence of the ferromagnetic components. Surprisingly, the peaks below T_N have no correlation with those observed below T_N (= 115 K) in the dc susceptibility measurements (∼89 and 71 K); see also Figure S1. A more

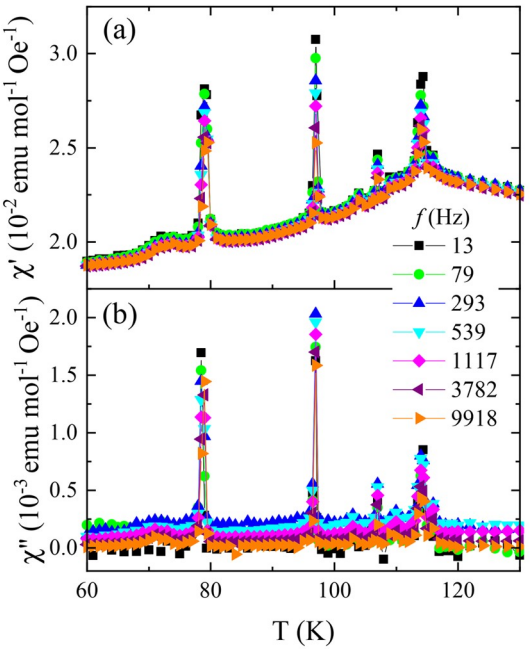

Figure 3. Temperature dependence of (a) the real χ' and (b) the imaginary χ'' components of the ac susceptibility measured at various frequencies and zero dc bias field.

careful inspection of the ac susceptibility data reveals a weak, broad peak at 73 K in χ' (71 K in χ'') in Figure 4, which can be associated with the low-temperature peak (71 K) observed in the dc measurement. However, the 89 K peak is still invisible in the ac susceptibility.

Figure 4 shows the dc field dependence of the ac susceptibility at a fixed frequency of 3782 Hz. The sharp peaks at 107, 97, and 79 K are profoundly affected by dc fields and are almost completely suppressed with a dc field of 0.05 T,

https://doi.org/10.1021/acs.inorgchem.2c01293
Inorg. Chem. 2022, 61, 10880−10887

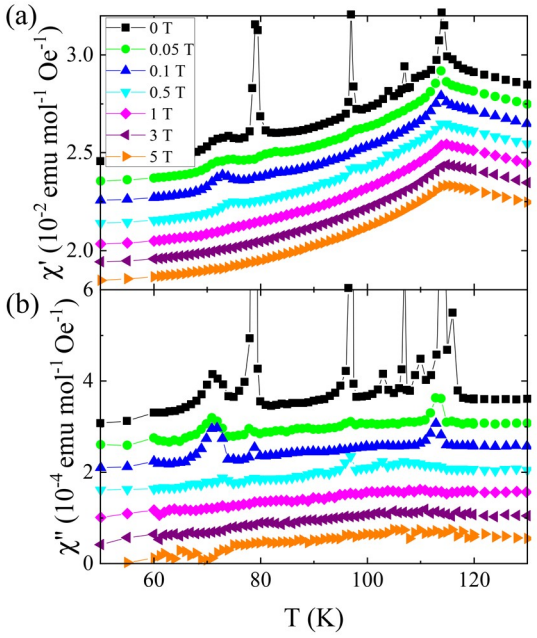

Figure 4. Temperature dependence of (a) the real χ' and (b) the imaginary χ'' components of the ac susceptibility measured at a frequency of 3782 Hz and various dc bias fields. The data has been shifted vertically for clarity.

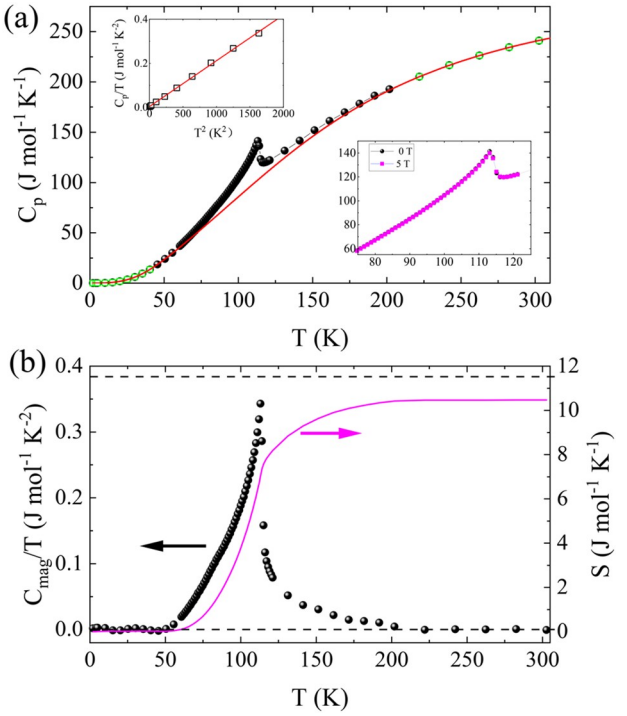

Figure 5. (a) Temperature dependence of the specific heat. The green data points are used for the estimation of the lattice contributions; see the text for details. The red curve is the fitting result according to the Debye and Einstein models. The left inset shows the low-temperature region and a fit with $C_p = \gamma T + \beta T^3$. The right inset compares the heat capacity measured at both zero and 5 T. (b) Magnetic heat capacity, C_{mag}/T, obtained by subtracting the calculated phonon contribution from the total heat capacity and the magnetic entropy obtained by integration of C_{mag}/T. The upper dashed line indicates the expected entropy value of $2R$ ln2 (the factor of 2 comes from the two Co ions in the chemical formula).

whereas the 71 K peak persists to 0.1 T. Above 0.5 T, only the signature of T_N survives, which behaves as a kink in χ', has no anomaly in χ'', and does not change in fields up to 5 T, consistent with an antiferromagnetic transition.

Specific Heat. The specific heat, C_p, is presented in Figure 5a. A λ-shaped transition can be observed at T_N = 115 K. No further anomaly is observed at lower temperatures. The transition at 115 K is very robust to the magnetic field; no obvious changes can be observed at 5 T, as shown in the right inset and consistent with the ac susceptibility. The low-temperature (<40 K) region is described well by $C_p(T)/T = \gamma + \beta T^2$, yielding a negligibly small γ of 3(2) mJ/mol·K^2 and β of 2.08(2) × 10^{-4} J/mol·K^4, indicating that the low-temperature specific heat is dominated by phonon contributions. The Debye temperature, θ_D, extracted from $(12\pi^4 rR/5\beta)^{1/3}$, where r is the number of atoms in the chemical formula and R is the ideal gas constant, amounts to 482 K. In order to extract the magnetic contributions from the total heat capacity, the phonon contributions are estimated from a fit with a combination of the Debye and Einstein models

$$C_p(T) = x_D 9rR(T/\theta_D)^3 \int_0^{\theta_D/T} x^4 \exp(x)/[\exp(x) - 1]^2 \, dx + (1 - x_D)3rR(\theta_E/T)^2 \exp(\theta_E/T)/[\exp(\theta_E/T) - 1]^2 \quad (1)$$

using the high-temperature (>220 K) and low-temperature (<40 K) data points marked as green circles in Figure 5. The best fit results in about an x_D = 42% weight to the Debye term. The obtained Debye temperature, θ_D, amounts to 356 K, in reasonable agreement with the one extracted from the low-temperature fitting alone, while the Einstein temperature, θ_E, is 620 K. The magnetic contribution, C_{mag}, is thus obtained by subtracting the fitted phonon contribution from the total heat capacity, and the magnetic entropy is then calculated by integrating C_{mag}/T, as shown in Figure 5. The calculated release of entropy is about 10.5 J/mol·K, which is close to the value expected for an effective spin $s = {}^1/_2$ state [$2R$ ln($2s$ + 1) = 11.52 J/mol·K].

Muon Spin Relaxation. In order to unravel the origin of the enigmatic magnetic behavior observed in the bulk, static, and dynamic susceptibility measurements, we have performed local-probed μSR measurements. Figure 6a shows the ZF-μSR time spectra measured at various temperatures. At 150 K, the spectrum exhibits a Gaussian-shaped depolarization behavior, indicating an electronic paramagnetic state, and the depolarization is mainly caused by the nuclear moments. With a decrease in temperature, the initial asymmetry drops quickly, showing a dramatic change in the spectra around T_N = 115 K. In the early time regions, Figure 6b exhibits clear muon spin precessions at low temperatures. At the base temperature (1.6 K), two independent components are required to describe the oscillating spectra, creating a beating; however, by T_N, the two frequencies become comparable and merge into one frequency (see the 110 K spectrum). In order to extract useful parameters from the spectra, a relaxation function

$$A(t) = A_0 G_{KT}(t) \exp(-\lambda_3 t) \quad (2)$$

was fit to the spectra above 110 K, where A_0 is the initial asymmetry at time zero, $G_{KT}(t)$ is the Gaussian Kubo−Toyabe function,[19] and λ_3 is the relaxation rate caused by electronic spins. At low temperatures, a three-component function

https://doi.org/10.1021/acs.inorgchem.2c01293
Inorg. Chem. 2022, 61, 10880−10887

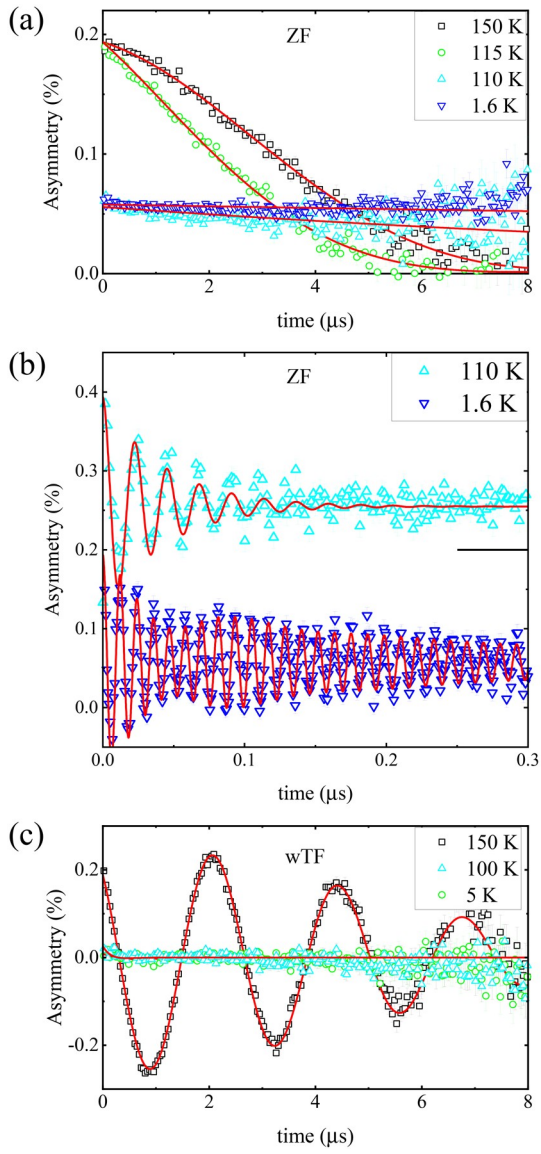

Figure 6. (a) Zero-field μSR spectra measured at various temperatures. (b) A closer look at the early time region showing the muon spin precessions at low temperatures. (c) Weak transverse field (wTF) spectra at various temperatures. Solid lines represent the fits with $A(t) = A_{TF}\cos(\gamma_\mu Bt + \varphi)\exp[-(\lambda t)^\beta]$.

$$A(t) = A_1\cos(\gamma_\mu B_1 t)\exp(-\lambda_1 t) + A_2\cos(\gamma_\mu B_2 t)\exp(-\lambda_2 t) + A_3\exp(-\lambda_3 t) \quad (3)$$

was used to describe the spectra, where A_i is the amplitude of each component with the constraint that $\sum_i A_i = A_0$, B_i is the internal field at the muon site, $\gamma_\mu/2\pi$ = 13.55 MHz/kOe is the gyromagnetic ratio of the muon, and λ_i is the corresponding relaxation rate for each component.

The temperature dependence of the extracted parameters is shown in Figure 7. Two internal fields can be resolved at the base temperature, and these remain almost constant until ~60 K. With the increase in temperature, the difference gets smaller and becomes indistinguishable around T_N, denoted as B_0 in Figure 7a. It is worth noting that the depolarization rate, λ_2, is almost 1 order larger than λ_1, indicating a much broader distribution for the B_2 component. The amplitudes for these two components, A_1 and A_2, are comparable over the whole

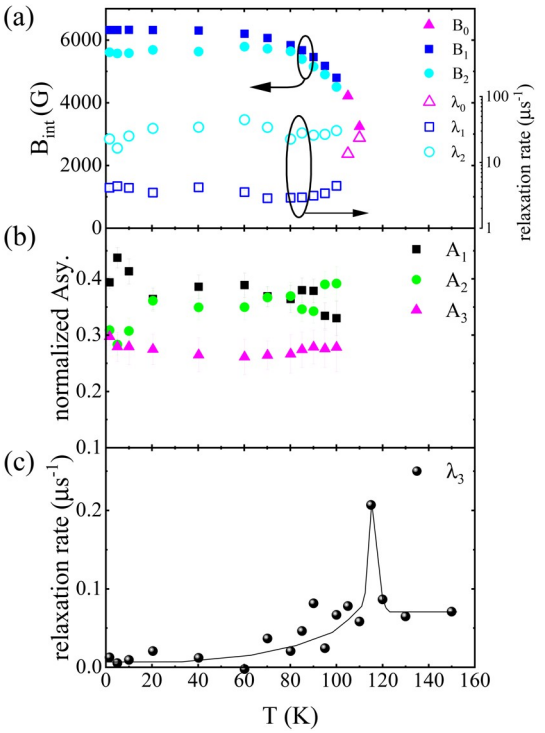

Figure 7. Temperature dependence of (a) the internal fields and corresponding relaxation rates, (b) the amplitude of different components, and (c) the slow relaxation rate. The solid line is a guide for the eyes.

temperature range. On the other hand, the fitted A_3 component, which reflects the portion of muons with the spin parallel to the internal fields, is ~0.3 at temperatures below 100 K, indicating that nearly 100% of the spin system is static.[20] This is further corroborated from the weak transverse field (wTF) measurement, as shown in Figure 6b. The paramagnetic volume fraction is proportional to the oscillation amplitude, and it is clearly seen that the oscillation amplitude is almost absent below 100 K. Finally, the magnetic transition temperature can also be inferred from the divergent behavior of λ_3, which reflects the critical slowing down of the electronic spins, and a sharp peak can be observed at 115 K, as shown in Figure 7c, consistent with the heat capacity and high-temperature magnetic transition.

Neutron Powder Diffraction. More insights into the magnetic ground state of this compound are obtained from neutron powder diffraction measurements. Figure 8a compares the neutron pattern measured just above the transition temperature and at the base temperature. Substantial magnetic intensities can be observed on top of the nuclear reflections, indicating a $\mathbf{k}$ = 0 propagation vector. No qualitative difference is observed in the intermediate temperature range (data not shown). The magnetic structure was determined with the aid of irreducible representation analysis using the BasIreps program. For the Co ions at the 16g site with space group *Fddd* and propagation vector $\mathbf{k}$ = 0, the magnetic reducible representation is decomposed into eight irreducible representations (IRs). The basis vectors for each IR can be found in Table S1. The complexity due to stacking faults, as will be discussed later, and the mixing valence state of the Co ions are neglected during the refinement. Therefore, the obtained magnetic structure should be considered as an averaged one.

https://doi.org/10.1021/acs.inorgchem.2c01293
Inorg. Chem. 2022, 61, 10880−10887

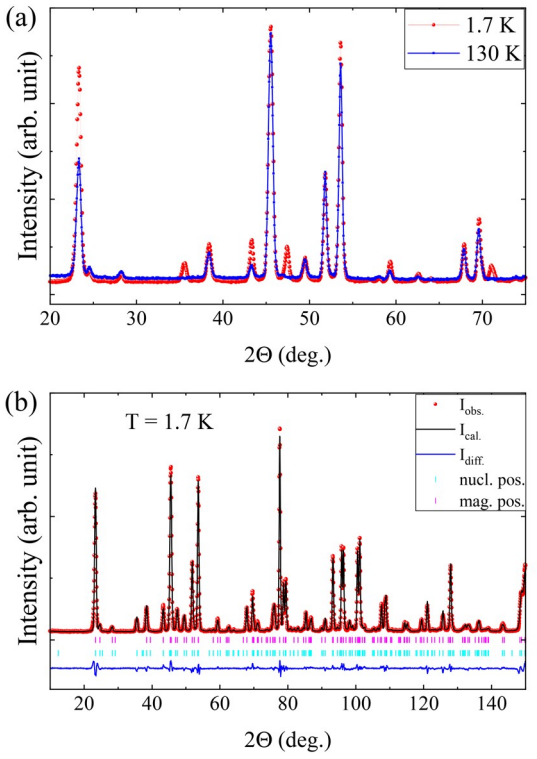

Figure 8. (a) Comparison of the neutron powder diffraction patterns measured above and below the transition temperature. A neutron wavelength of 1.89 Å was selected for the measurements. (b) Rietveld magnetic structure refinement against the neutron pattern according to the irreducible representation Γ_1. The best fit yields R_{mag} = 5.70%.

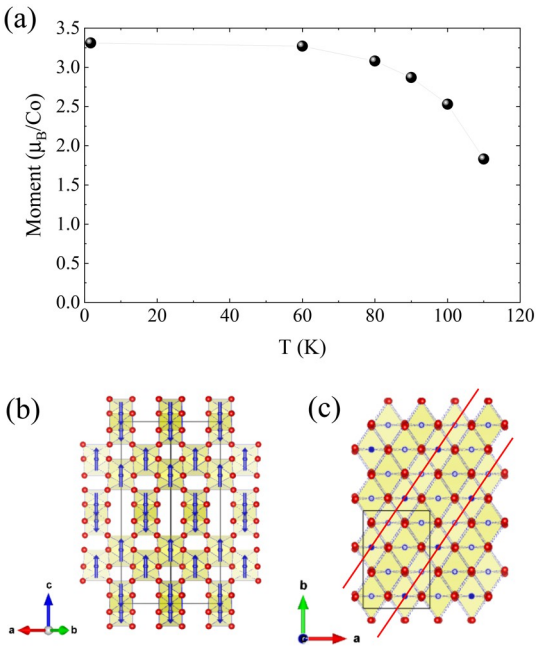

Figure 9. (a) Temperature dependence of the Co moments extracted from Rietveld refinement. (b and c) The magnetic structure looked at from different directions. In panel c, the red lines indicate possible missing layers due to the stacking faults. The blue and white circles represent the spins pointing along the $+c$ and $-c$ directions, respectively.

Finally, it was found that only the IR Γ_1 can describe the pattern satisfactorily. The refined pattern is shown in Figure 8, and the temperature dependence of the moment size of the Co ion is presented in Figure 9a. The Co moments are pointing either parallel or antiparallel to the c-axis. The moments along the zigzag chains are coupled ferromagnetically, while the interchain moments are coupled antiferromagnetically, following the Goodenough–Kanamori rules.[21] Note that the moment size at the base temperature amounts to 3.31 μ_B/Co, which is larger than the spin-only value for the high-spin state of Co^{2+} (3 μ_B), consistent with the expectation that substantial orbital moments are not quenched from the high-temperature Curie–Weiss fitting.

DISCUSSION

The most striking observation for orthorhombic $Li_3Co_2SbO_6$ is the presence of multiple transitions below T_N from the dc and ac susceptibility measurements. These transitions have the following characteristics: (1) they are ferromagnetic, although the overall ground state is antiferromagnetic; (2) they are quite soft and can be easily suppressed by a modest magnetic field; (3) they are not detected by other measurements such as heat capacity, μSR, and neutron diffraction. These results suggest that these transitions originate from a minor part of the sample and are reminiscent of transitions seen in the layered manganites $La_{2-2x}Sr_{1+2x}Mn_2O_7$ (x = 0.4), for which the ground state is ferromagnetic with $T_c \sim 125$ K but an additional ferromagnetic feature is observed near room temperature that is also suppressed, or masked, by an applied magnetic field[22] and is attributed to stacking faults of the perovskite layers[23] and other members of the Ruddlesden–Popper series. These peaks are also reminiscent of the multiple transitions observed in α-$RuCl_3$ due to stacking faults of the honeycomb layers.[24] Such a stacking faults scenario is also plausible for the $Li_3Co_2SbO_6$ case. From Figure 9c, one sees that the close-packed anion layers are stacked either along the [110] or the [1−10] direction and the Co ions are sandwiched between these layers. If some of the layers, as indicated by the red lines, are missing, ferromagnetic regions could appear.

There could be other possibilities such as antisite disorder between the Li and Co ions, as proposed by Brown et al.,[11] or the coexistence of Co^{2+} and Co^{3+} ions as found by our refinement. In both cases, the appearance of Li or Co^{3+} ions at the Co^{2+} site could disturb the long-range magnetic ordering. For example, as shown in Figure 9b, the zigzag chains running along the [110] and [1−10] directions are connected by corner-shared CoO_6 octahedra, which favors an antiferromagnetic interaction between the chains. If one of the Co^{2+} ions mediating this interchain interaction is missing, the local structure around this defect may become ferromagnetic. Finally, the real situation could be a complicated combination of these individual effects.

The stacking faults or local site disorders may be inferred from the μSR results. In Figure 7a, the relaxation rate, which is proportional to the internal field distribution width, corresponding to the internal field B_2, is much larger than that of B_1. It can be surmised that muons that stopped around the stacking faults or local disorders contribute to the B_2 component, while those far from the defects contribute to the B_1 component, as was observed in Na_2IrO_3.[13] Note that the amplitudes of A_1 and A_2 are comparable, which seems to contradict the conjecture that the ferromagnetic component only has a minor volume fraction. The argument is that the

https://doi.org/10.1021/acs.inorgchem.2c01293
Inorg. Chem. 2022, 61, 10880−10887

muons feel the field distribution via a long-range dipolar field, which extends over the ferromagnetic boundaries. On the other hand, the possibility that there exist two inequivalent muon sites with similar populations cannot be ruled out; future density functional theory (DFT) calculations will be helpful to clarify this point.

Another enigmatic phenomenon is the distinct transition temperature observed by ac and dc magnetic susceptibility measurements. One possibility is the different amplitudes of the magnetic fields applied during the measurement with the pinning barriers for the domains being too high for the ac measurement, as observed in the ferrimagnetic system $FeCr_2S_4$.[25] Nevertheless, unexplained differences between static and dynamic susceptibility are rare, and the origins are still open.

CONCLUSIONS

The magnetic properties of orthorhombic $Li_3Co_2SbO_6$ have been studied in detail by means of dc and ac susceptibility, muon spin relaxation, and neutron diffraction measurements. The sample forms an antiferromagnetic ground state, with ferromagnetic chains stacked antiferromagnetically along the *c*-axis. Additional transitions below T_N are observed by dc and ac magnetic susceptibility measurements, which are ascribed to possible stacking faults and/or local disorders, resulting in a ferromagnetic component within the overall antiferromagnetic matrix. However, single-crystal studies probing the local magnetic and crystallographic structure are required to fully understand the magnetic response in orthorhombic $Li_3Co_2SbO_6$. Those findings are also suggestive for the honeycomb phase in which the honeycomb layers are prone to stacking faults, either nuclear structurally or magnetically, which may not be readily detected by bulk structural measurements.

ASSOCIATED CONTENT

Supporting Information

The Supporting Information is available free of charge at https://pubs.acs.org/doi/10.1021/acs.inorgchem.2c01293.

Additional experimental measurements and magnetic symmetry analysis (PDF)

Accession Codes

CCDC 2179100 contains the supplementary crystallographic data for this paper. These data can be obtained free of charge via www.ccdc.cam.ac.uk/data_request/cif, or by emailing data_request@ccdc.cam.ac.uk, or by contacting The Cambridge Crystallographic Data Centre, 12 Union Road, Cambridge CB2 1EZ, U.K.; fax: +44 1223 336033.

AUTHOR INFORMATION

Corresponding Authors

Yuke Li − *School of Physics and Hangzhou Key Laboratory of Quantum Matters, Hangzhou Normal University, Hangzhou 311121, China*; Email: yklee@hznu.edu.cn

Hanjie Guo − *Neutron Science Platform, Songshan Lake Materials Laboratory, Dongguan, Guangdong 523808, China*; orcid.org/0000-0001-6203-5557; Email: hjguo@sslab.org.cn

Authors

Qianhui Duan − *School of Physics and Hangzhou Key Laboratory of Quantum Matters, Hangzhou Normal University, Hangzhou 311121, China; Neutron Science Platform, Songshan Lake Materials Laboratory, Dongguan, Guangdong 523808, China*

Huanpeng Bu − *Neutron Science Platform, Songshan Lake Materials Laboratory, Dongguan, Guangdong 523808, China*

Vladimir Pomjakushin − *Laboratory for Neutron Scattering and Imaging, Paul Scherrer Institute, CH-5232 Villigen, Switzerland*

Hubertus Luetkens − *Laboratory for Muon Spin Spectroscopy, Paul Scherrer Institute, CH-5232 Villigen, Switzerland*

Jinkui Zhao − *Neutron Science Platform, Songshan Lake Materials Laboratory, Dongguan, Guangdong 523808, China*

Jason S. Gardner − *Material Science and Technology Division, Oak Ridge National Laboratory, Oak Ridge, Tennessee 37831, United States*

Complete contact information is available at: https://pubs.acs.org/10.1021/acs.inorgchem.2c01293

Author Contributions

#Q.D. and H.B. contributed equally to this work.

Notes

The authors declare no competing financial interest.

ACKNOWLEDGMENTS

H.G. acknowledges the support from the NSF of China, Grant No. 12004270, and the Guangdong Basic and Applied Basic Research Foundation (2019A1515110517). This research is also partly supported by the NSF of China, Grant No. U1932155. A portion of this work was supported by the Laboratory Directed Research and Development (LDRD) program of Oak Ridge National Laboratory, managed by UT-Battelle, LLC for the U.S. Department of Energy.

REFERENCES

(1) Liu, H.; Khaliullin, G. Pseudospin exchange interactions in d^7 cobalt compounds: Possible realization of the Kitaev model. *Phys. Rev. B* **2018**, *97*, 014407.

(2) Sano, R.; Kato, Y.; Motome, Y. Kitaev-Heisenberg Hamiltonian for high-spin d^7 Mott insulators. *Phys. Rev. B* **2018**, *97*, 014408.

(3) Xiao, G.; Xia, Z.; Zhang, W.; Yue, X.; Huang, S.; Zhang, X.; Yang, F.; Song, Y.; Wei, M.; Deng, H.; Jiang, D. Crystal Growth and the Magnetic Properties of $Na_2Co_2TeO_6$ with Quasi-Two-Dimensional Honeycomb Lattice. *Cryst. Growth Des.* **2019**, *19*, 2658−2662.

(4) Yan, J. Q.; Okamoto, S.; Wu, Y.; Zheng, Q.; Zhou, H. D.; Cao, H. B.; McGuire, M. A. Magnetic order in single crystals of $Na_3Co_2SbO_6$ with a honeycomb arrangement of $3d^7$ Co^{2+} ions. *Phys. Rev. Materials* **2019**, *3*, 074405.

(5) Liu, H.; Chaloupka, J.; Khaliullin, G. Kitaev Spin Liquid in 3d Transition Metal Compounds. *Phys. Rev. Lett.* **2020**, *125*, 047201.

(6) Songvilay, M.; Robert, J.; Petit, S.; Rodriguez-Rivera, J. A.; Ratcliff, W. D.; Damay, F.; Balédent, V.; Jiménez-Ruiz, M.; Lejay, P.; Pachoud, E.; Hadj-Azzem, A.; Simonet, V.; Stock, C. Kitaev interactions in the Co honeycomb antiferromagnets $Na_3Co_2SbO_6$ and $Na_2Co_2TeO_6$. *Phys. Rev. B* **2020**, *102*, 224429.

(7) Yao, W.; Li, Y. Ferrimagnetism and anisotropic phase tunability by magnetic fields in $Na_2Co_2TeO_6$. *Phys. Rev. B* **2020**, *101*, 085120.

(8) Lin, G.; Jeong, J.; Kim, C.; Wang, Y.; Huang, Q.; Masuda, T.; Asai, S.; Itoh, S.; Gunther, G.; Russina, M.; et al. Field-induced quantum spin disordered state in spin-1/2 honeycomb magnet $Na_2Co_2TeO_6$. *Nat. Commun.* **2021**, *12*, 5559.

(9) Lefrançois, E.; Songvilay, M.; Robert, J.; Nataf, G.; Jordan, E.; Chaix, L.; Colin, C. V.; Lejay, P.; Hadj-Azzem, A.; Ballou, R.;

Simonet, V. Magnetic properties of the honeycomb oxide $Na_2Co_2TeO_6$. *Phys. Rev. B* **2016**, *94*, 214416.
(10) Bera, A. K.; Yusuf, S. M.; Kumar, A.; Ritter, C. Zigzag antiferromagnetic ground state with anisotropic correlation lengths in the quasi-two-dimensional honeycomb lattice compound $Na_2Co_2TeO_6$. *Phys. Rev. B* **2017**, *95*, 094424.
(11) Brown, A. J.; Xia, Q.; Avdeev, M.; Kennedy, B. J.; Ling, C. D. Synthesis-Controlled Polymorphism and Magnetic and Electrochemical Properties of $Li_3Co_2SbO_6$. *Inor. Chem.* **2019**, *58*, 13881−13891.
(12) Cao, H. B.; Banerjee, A.; Yan, J. Q.; Bridges, C. A.; Lumsden, M. D.; Mandrus, D. G.; Tennant, D. A.; Chakoumakos, B. C.; Nagler, S. E. Low-temperature crystal and magnetic structure of α-$RuCl_3$. *Phys. Rev. B* **2016**, *93*, 134423.
(13) Choi, S. K.; Coldea, R.; Kolmogorov, A. N.; Lancaster, T.; Mazin, I. I.; Blundell, S. J.; Radaelli, P. G.; Singh, Y.; Gegenwart, P.; Choi, K. R.; Cheong, S.-W.; Baker, P. J.; Stock, C.; Taylor, J. Spin Waves and Revised Crystal Structure of Honeycomb Iridate Na_2IrO_3. *Phys. Rev. Lett.* **2012**, *108*, 127204.
(14) Vivanco, H. K.; Trump, B. A.; Brown, C. M.; McQueen, T. M. Competing antiferromagnetic-ferromagnetic states in a d^7 Kitaev honeycomb magnet. *Phys. Rev. B* **2020**, *102*, 224411.
(15) Suter, A.; Wojek, B. M. Musrfit: A Free Platform-Independent Framework for μSR Data Analysis. *Physics Procedia* **2012**, *30*, 69−73.
(16) Rodríguez-Carvajal, J. Recent advances in magnetic structure determination by neutron powder diffraction. *Physica B* **1993**, *192*, 55−69.
(17) Guo, H.; Zhao, L.; Baenitz, M.; Fabrèges, X.; Gukasov, A.; Melendez Sans, A.; Khomskii, D. I.; Tjeng, L. H.; Komarek, A. C. Emergent 1/3 magnetization plateaus in pyroxene $CoGeO_3$. *Phys. Rev. Res.* **2021**, *3*, L032037.
(18) Guo, H.; Manna, K.; Luetkens, H.; Hoelzel, M.; Komarek, A. C. Spin glass behavior in $LaCo_{1-x}Rh_xO_3$ (x = 0.4, 0.5, and 0.6). *Phys. Rev. B* **2016**, *94*, 205128.
(19) Guo, H.; Tanida, H.; Kobayashi, R.; Kawasaki, I.; Sera, M.; Nishioka, T.; Matsumura, M.; Watanabe, I.; Xu, Z.-a. Magnetic instability induced by Rh doping in the Kondo semiconductor $CeRu_2Al_{10}$. *Phys. Rev. B* **2013**, *88*, 115206.
(20) For powder samples in the magnetic ordered state, one-third of the implanted muon spins will be parallel to the internal fields. This component can be relaxed by a spin−lattice relaxation process, resulting in a slowly decaying 1/3 tail.
(21) Kanamori, J. Superexchange interaction and symmetry properties of electron orbitals. *J. Phys. Chem. Solids* **1959**, *10*, 87−98.
(22) Seshadri, R.; Hervieu, M.; Martin, C.; Maignan, A.; Domenges, B.; Raveau, B.; Fitch, A. N. Study of the Layered Magnetoresistive Perovskite $La_{1.2}Sr_{1.8}Mn_2O_7$ by High-Resolution Electron Microscopy and Synchrotron X-ray Powder Diffraction. *Chem. Mater.* **1997**, *9*, 1778−1787.
(23) Moreno, N. O.; Pagliuso, P. G.; Rettori, C.; Gardner, J. S.; Sarrao, J. L.; Thompson, J. D.; Huber, D. L.; Garcia-Flores, A.; Oseroff, S. B. Extrinsic and intrinsic features above T_C in layered Manganite: $La_{1.2}Sr_{1.8}Mn_2O_7$. *Physica B* **2000**, *292*, 1−8.
(24) Yamauchi, I.; Hiraishi, M.; Okabe, H.; Takeshita, S.; Koda, A.; Kojima, K. M.; Kadono, R.; Tanaka, H. Local spin structure of the α − $RuCl_3$ honeycomb-lattice magnet observed via muon spin rotation/relaxation. *Phys. Rev. B* **2018**, *97*, 134410.
(25) Tsurkan, V.; Hemberger, J.; Klemm, M.; Klimm, S.; Loidl, A.; Horn, S.; Tidecks, R. Ac susceptibility studies of ferrimagnetic $FeCr_2S_4$ single crystals. *J. Appl. Phys.* **2001**, *90*, 4639−4644.

https://doi.org/10.1021/acs.inorgchem.2c01293
Inorg. Chem. 2022, 61, 10880−10887